THERMO-PHYSICAL PROPERTIES OF AS DEPOSITED AND AGED THERMAL BARRIER COATINGS (TBC) FOR GAS TURBINES: STATE-OF-THE ART AND ADVANCED

Federico Cernuschi[1], Paolo Bison[2], Daniel E. Mack[3], Marco Merlini[4], Stefano Boldrini[5], Stefano Marchionna[1], Stefano Capelli[1],Stefano Concari[1], Alessia Famengo[5], Alessandro Moscatelli[6], Werner Stamm[7]

[1] RSE Via Rubattino 54, 20134 Milano Italy

[2] CNR-ITC, C.so Stati Uniti 4, 35127 Padova, Italy

[3] Forschungszentrum Jülich GmbH, 52425 Jülich, Germany

[4] Università degli Studi di Milano, Dipartimento Scienze della Terra "Ardito Desio", via Mangiagalli 23, 20133 Milano,

[5] CNR-ICMATE, C.so Stati Uniti 4, 35127 Padova, Italy

[6] Flame Spray Via Leonardo Da Vinci 30, 20877 Roncello (MB) Italy

[7] Siemens AG, Mellinghofer Str. 55, 45473 Mülheim an der Ruhr, Deutschland

Abstract

In the perspective of fuelling the future generations of gas turbines by hydrogen rich syngas, the evaluation of the effect of a higher water vapour content into the flue gases on the coatings used, or potentially usable, for protecting the hot path is a need. For this purpose, state-of-the-art YPSZ APS TBC with two different microstructures have been exposed for 500 hours at different temperatures in the range 1000°C – 1250°C either in air and air+20% H_2O. The comparison between the different testing conditions has been performed in terms of sintering kinetics and phase stability, as evaluated by thermal diffusivity measurements and Synchrotron X-Rays diffraction, respectively. Furthermore the characterisation of thermal properties of two innovative TBCs (GZO-YPSZ and YAG) potentially able to withstand the CMAS attack and erosive environments, respectively, has been carried out.

The main outcomes of this experimental activity did not provide any clear evidence of a different behaviour of TBC, at least in the aging time (500h) and temperature (1000°C-1250°C) range considered in the frame of this work.

As concerns advanced TBC, thermal conductivity of YSZ-GZO samples are affected mainly by the microstructure and only to a lesser extent by the chemical composition. YAG TBC with the peculiar brick-like microstructure exhibits a high thermal conductivity, compared to YSZ and GZO-YPSZ TBCs.

1. INTRODUCTION

Owing to climate changes, greenhouses gases emitted by fossil fuelled power generation plants should be drastically reduced. On the other hand, power plants are still necessary to guarantee the grid stability when the share of non-programmable renewables is predominant and enable the transition towards a green power generation waiting for economically feasible energy storage technologies, such as electrochemical, mechanical, thermal and gravitational. In this perspective, Carbon Capture and Sequestration (CCS) is an viable option to minimise CO_2 emissions. Among the different potentially applicable solutions, pre-combustion CCS is attractive because of the low energy consumption.

Integrated Gasification Combined Cycle (IGCC) is currently one of the most attractive technologies for the high-efficiency use of coal. It enables the conversion of coal and other solid or liquid fuels to a gaseous syngas fuel, while still maintaining aggressive emissions targets and high efficiency. Pre-combustion methods are the preferred means of capturing CO_2 in IGCC systems. An IGCC plant equipped with pre-combustion CO_2 capture combined with low emissions of other gases, e.g. NOx, SOx, can be realised through major advancement in IGCC gas turbine technology.

The main aim of this future technology is to use an undiluted hydrogen-rich syngas as fuel, consequently, water vapour formed from H_2 in the combustion process along with differences in water input for various gasification processes (e.g. dry feed v. wet feed) result in significant differences in water vapour levels in the combustion gases flowing through IGCC turbine hot sections.

This can result in differences in hot section component degradation since increased water vapour levels have increased oxidation rates in laboratory tests of turbine materials [1].

Recently, B. Pint et al, M.H. Sullivan et al and W. Nowak experimentally studied the effect of the increased steam content on TBC life [2-7].

In particular, Pint and co-workers observed a significant reduction of Air Plasma Spray (APS) TBC life by cyclic oxidation tests when testing environment changed from dry air to air+10% water vapour. On the other hand, a further increase of water vapour to 50% did not affect TBC life significantly. Although no obvious impact on bondcoat and thermally grown oxide composition and microstructure was relieved after TBC failure in most of the cases, when exposition time was sufficiently long, some differences in TGO microstructure and TBC failure modes were observed providing some indications to explain the outcomes in terms of TBC lives [2]. When samples without the ceramics top layer were considered, any clear effect of water vapour content on TGO was noticed [3]. Furthermore in Pt-diffusion and Pt- modified aluminide bondcoats, in air+10% water vapour more θ-Al_2O_3 formation and small alumina morphology and microchemistry differences compared to dry air are reported [4,5].

M.H. Sullivan and D. R. Mumm observed that at early oxidation stages the presence of higher water vapour partial pressures promoted and enhanced the $(Ni, Co)(Al, Cr)_2O_4$ spinel formation, on top of Co/Cr rich phases (γ phase) and even in correspondence to Al rich phase (β-phase) that is supposed to affect at later stages the bondcoat stability, the TGO development and TBC lifetime [6].

W. Nowak argued that the observed lifetime shortening by water vapour (20%) on APS TBC samples could be correlated with an effect of water vapour on crack propagation in the ceramic topcoats. The proposed explanation was that the non-uniform Y distribution across powder particles could promote and enhance the transformation from tetragonal to monoclinic zirconia in the presence of water vapour at temperature below approximately 400°C during cooling [7].

The aim of this work is to evaluate, if any, the effect of water vapour content in the flue gases on the state-of-the-art TBC in terms of sintering kinetics and/or phase stability by using thermo-physical and synchrotron radiation diffraction, respectively.

Furthermore, thermo-physical characterisation of advanced TBCs candidated for future applications also in next IGCC generation gas turbine hot path has been provided, as well. In particular, a two-phase TBC made of Gadolinium Zirconate (GZO) and YPSZ and a two-layer TBC made of YAG-YPSZ have been selected as potentially able to withstand CMAS attack and erosive environments [8,9].

2. EXPERIMENTAL

As representatives of YPSZ state-of-the art TBC one highly porous and one dense vertically cracked TBC have been selected.

2.1 Sample deposition

Highly porous and dense highly cracked YPSZ APS TBC

The powder for spraying freestanding coatings is a standard commercial ZrO_2-$7Y_2O_3$ TBC (Amperit 827 produced by H.C.Starck). The TBC porosity (see Figure 1 and Table I) measured by Image Analysis (IA) on as sprayed highly porosity and dense highly cracked samples resulted equal to an average value of 25-30% and 3 – 4%, respectively.
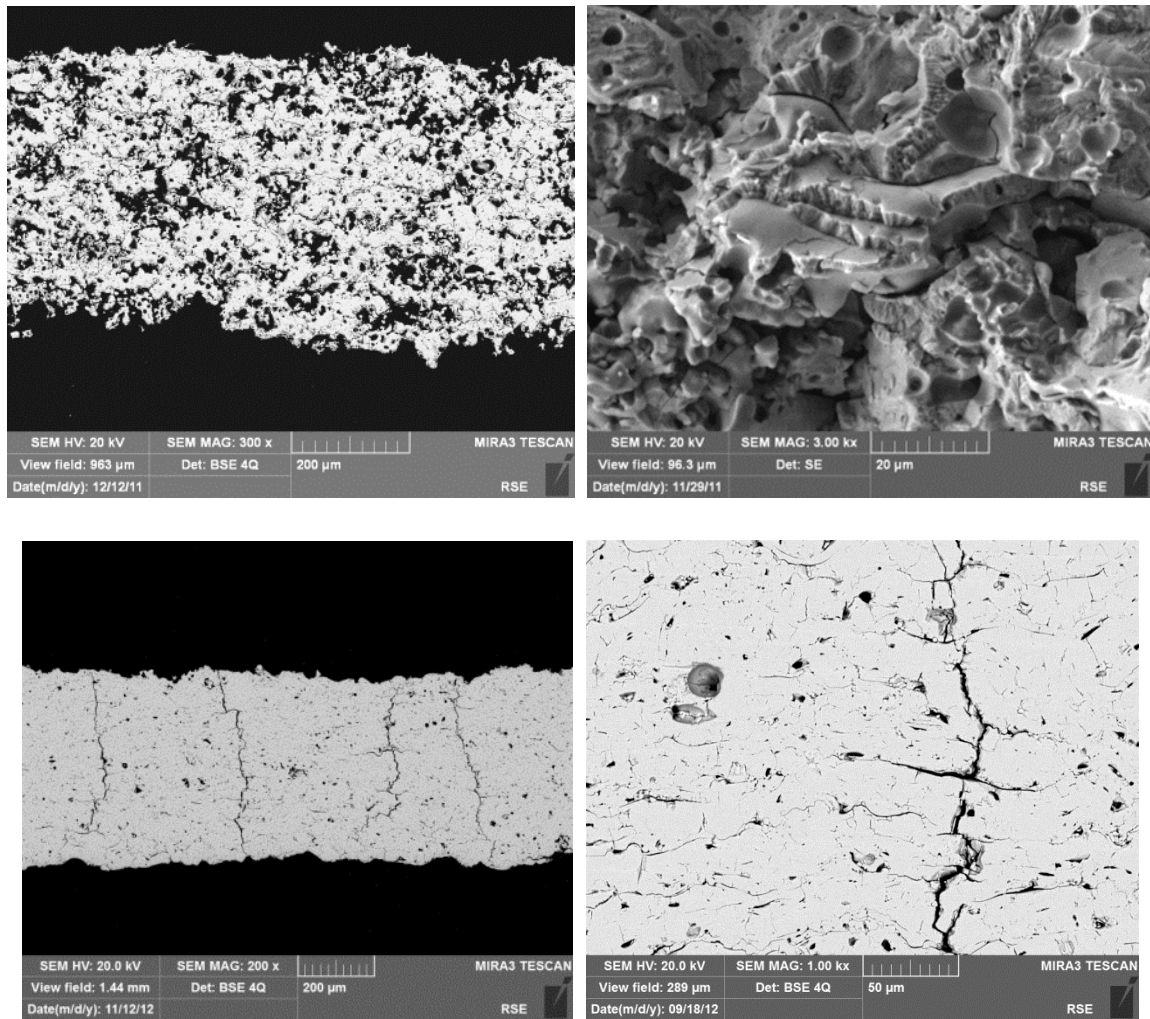
Figure 1 – Microstructure of state-of-the-art TBCs. (a)-(b) Highly porous TBC and (c)-(d) dense highly cracked TBC .

Single YSZ-GZO composite and bilayer TBC of porous YSZ with top layer of YSZ-GZO composite

The single layer YSZ-GZO consists of a layer of ceramic composite from 8YSZ with gadolinium zirconate (GZO) of 500±50 μm thickness deposited with standard Atmospheric Plasma Spray (APS) equipment (Oerlikon Metco TriplexPro-210™). The ceramic bilayer consists two layers 250±50 μm each; the internal layer is made of 8YSZ and an outer layer is nominally identical to the single layer composite. Powders used have been commercially available HOSP 8YSZ (Metco™ 204NS) and a blend of same 8YSZ powder with GZO powder of spherical shape (proprietary specification produced by H.C. Starck), respectively. Figure 2 shows the SEM images of the microstructures of these advanced TBCs. Porosity resulted in the range 14-16% and 15-18% for single a bilayer samples, respectively. The GZO phase ranges from 42 - 47% and from 23 – 27% for single and bilayer TBCs (see Table II).
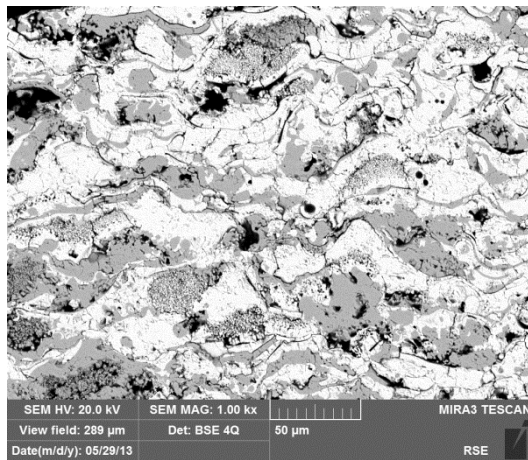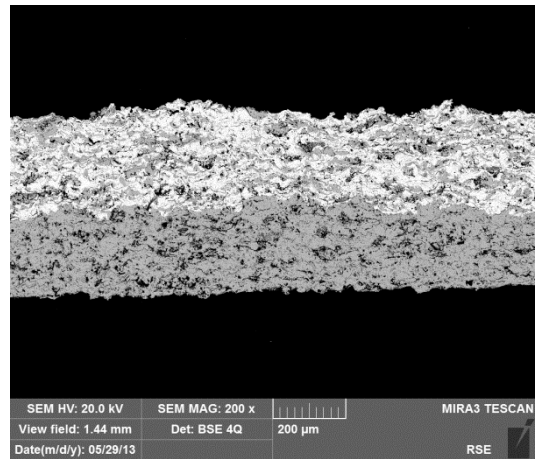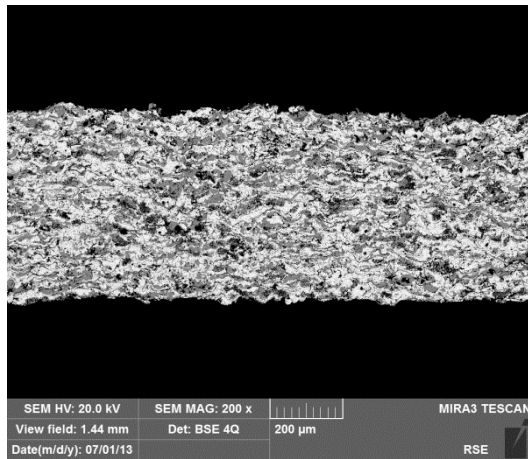
Figure 2 – Image of (a) single YSZ-GZO composite and (b) bilayer YSZ/YSZ-GZO composite. (c) high magnification image of YSZ-GZO composite; the white (GZO) and grey (YSZ) phases can be clearly distinguished.

YAG

The single YAG TBCs samples have been deposited with standard APS equipment (Oerlikon Metco TriplexPro-210™). The powder was synthesized by Treibacher (Austria) and agglomerated by spray drying at Forschungszentrum Jülich, respectively. By suitable spraying parameters a peculiar brick-like structure has been obtained, as pointed out in Figure 3.
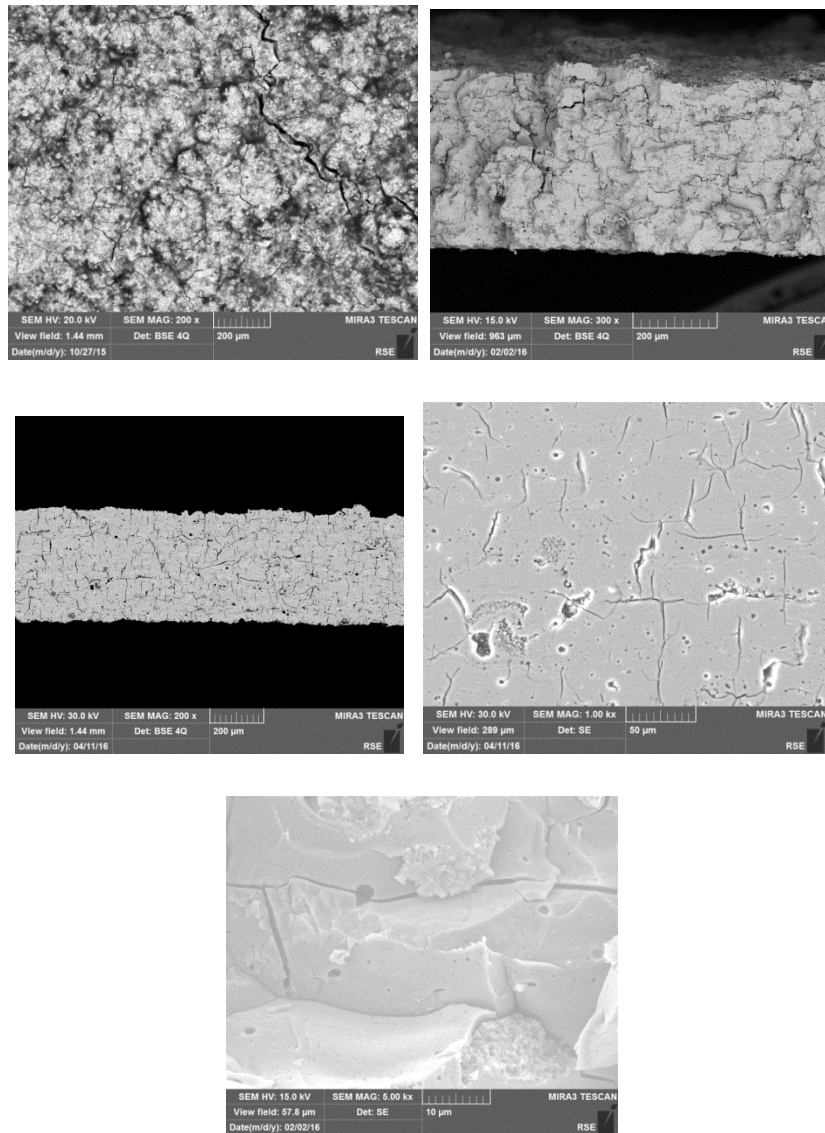
Figure 3 – YAG TBC. Image of (a) Top surface, (b) fracture surface and (c-e) section at different magnifications. The peculiar brick-like structure can be clearly observed.

State of the art YPSZ TBC samples have been aged in air (R286&R320) and in air+20% steam (R287&R267) at temperatures ranging from 1000°C up to 1250°C for 500 hours. Advanced YPSZ+GZO TBCs have been characterised both in as sprayed conditions and after heat treatment in air at temperatures ranging from 1000°C up to 1250°C for 500 hours. As concerns YAG TBCs measurements have been performed both before and after an heat treatment (900°C for 24 hours) finalised to promote the transition from amorphous to crystalline.

2.1 Microstructural characterisation

The microstructural characterisation of TBCs was performed by scanning electron microscopy (SEM) (MIRA XMH, Tescan, Brno, CK). TBC specimens were impregnated in vacuum using epoxy resin. The TBC thickness has been evaluated as the average of 30 values measured by (IA) (Screen Measurement, Laboratory Imaging Ltd., Praha, CZ) along the whole sample section. The overall porosity has been evaluated from ten 700x back-scattered electron images (BEI) taken along each sample cross-section.

Pores have been classified depending on their elongation e (defined as the ratio between the maximum and the minimum Feret diameters of the object) and orientation in respect to the heat flux direction. In particular, as explained in details elsewhere, all pores having an elongation $e \leq 2$ have been considered as "spherical" while those with $e > 2$ have been considered lamellar shaped [10].

For dual phase samples, the volumetric fraction of the both phases have been estimated by BEI images used for porosity evaluation .

Table I and Table II summarise the name of samples, the main microstructural parameters (i.e. overall thickness and porosity, as measured by IA) and the heat treatment for the state-of-the-art and the advanced TBC samples, respectively. Furthermore, Table III and IV summarise detailed microstructural features, as well as phase composition for the state-of-the-art and advanced GZO+YPSZ and YAG samples, respectively.

2.2 XRD and Synchrotron radiation diffraction

X-ray diffraction data were collected with laboratory and synchrotron X-ray diffraction. Laboratory X-ray experiments were performed with a four circle diffractometer equipped with CCD detector (Oxford X'Calibur, University of Milano) and Mo X-ray source. Surface and bulk experiments were conducted. The results allowed a preliminary sample characterisation. High-resolution diffraction on YPSZ samples, was conducted with synchrotron diffraction, at the Elettra synchrotron, (Trieste, Italy) at the MCX beamline. The experiments have been performed with monochromatic radiation (λ=0.7866 Å), in transmission geometry, using the standard beamline setup [11]. The measured samples with synchrotron radiation, consisted into fragments (apx. 1 mm^3) representative of the bulk ceramic materials, without grinding to prevent any phase change and conserve microstructure

features. The laboratory 2D diffraction data indicate good homogeneity in intensity distribution in the diffraction rings, suggesting negligible texture effects in the sample. The high-resolution data were analysed with Rietveld method using the GSAS-Expgui software [12, 13]. The analysis was conducted using the tetragonal, cubic and monoclinic zirconia model, with starting lattice parameters calculated preliminarily, following the calibration reported in Krogstad et al [14]. The Rietveld analysis provide, for each sample, refined lattice parameters for all the zirconia polymorphs, and quantitative estimation of the phase abundances.

2.3 Thermal diffusivity and specific heat of state-of the art and advanced TBC

2.3.1 THE MEASUREMENT TECHNIQUES

Laser flash

The through-the-thickness thermal diffusivity of all the freestanding TBC samples was measured by the Laser Flash technique [15, 16] using two different equipments (LFA 427 Netzsch-Geratebau GmbH, Selb, Germany and Theta Industries Inc., Port Washington, NY, USA). At RT, Laser flash measurements have been performed in air and in vacuum (<0.01 Pa). Measurements were repeated five times in each condition, for improving the precision of measurement. Typical accuracy for Laser Flash technique is 2-5%.

At high temperatures thermal diffusivity have been measured in vacuum and/or in inert atmosphere (Ar),only on few samples, as summarised in Table V and VI.

Owing to the TBC translucency, prior to evaluating the thermal diffusivity, thin layers of graphite were painted on both sample surfaces, respectively to make the TBC front face opaque to the Nd:YAG laser radiation (1.06 μm) and to increase the rear face emissivity in the IR detector [10].

Thermal diffusivity has been estimated from the experimental data of temperature vs. time by using standard equations and methods accounting for finite pulse duration and heat losses [17, 18].

Differential scanning calorimeter

Specific heat measurements were performed by Differential Scanning Calorimeter DSC 404 C (Netzsch-Geratebau GmbH, Selb, Germany). The scanning rate was 10°C/min in the temperature

range 100 up to 1100 °C. Measurements were carried out in argon atmospheres using platinum crucibles.

2.1.2. The state-of-the art TBC

Thermal diffusivity at RT in air and in vacuum

In this section only data referring to measurements carried out at RT in air and in vacuum are reported. As a matter of fact, data obtained at RT can provide several useful information on the TBC microstructure. First of all, the thermal diffusivity of as sprayed coatings gives an idea of what type of TBC is measured. Depending on their microstructure, for standard porous and vertically cracked TBC, typical values for RT thermal diffusivity measured in air are $2.5 - 4 \cdot 10^{-7}$ m²/s and $4.5 - 6 \cdot 10^{-7}$ m²/s, respectively [10, 19 , 20].

In this specific case, in agreement with the literature, as summarised by Table V, very porous (R286-1 and R286-5) and vertically cracked (R267-1) as sprayed TBCs show average thermal diffusivity values in air of $3.86 \cdot 10^{-7}$ m²/s and $4.82 \cdot 10^{-7}$ m²/s, respectively.

Another parameter that can be obtained is the ratio between thermal diffusivity measured in vacuum and in air $\eta = \alpha_{vacuum}/\alpha_{air}$. In fact, depending on the microstructure, η can change even significantly. The asymptotic value for η is 1. The pores that mainly contribute to this ratio are of course the open pores (those that are affected by having or not a medium inside). Among all the open pores, inter-lamellar pores laying in planes parallel to the TBC surface are those that mainly affect the through-the-thickness thermal diffusivity measured by the Laser Flash technique[1]. Furthermore, owing to the Knudsen effect[2] [23] graphically shown in Figure 4, the pores most sensitive to the gas inside them are those thicker than 0.1 μm. Thus low values (0.55 -0.65) of η means that there are very few closed pores and several lamellar shaped pores parallel to the surface with a thickness thicker than 0.1μm.

---

[1] For example the effect of spherical pores on the ratio $\alpha_{vacuum}/\alpha_{air}$ for a TBC having 25% spherical porosity with 3 μm diameter is 0.99. On the contrary, for a TBC with 10% of lamellar pores with 1 micron thickness and 1/40 aspect ratio, η is 0.31, according to the Bruggeman model [21, 22].

[2] The Knudsen effect consists in a significant drop of the thermal conductivity of a gas inside two planes when their distance is comparable to the mean free path of the gas molecules.
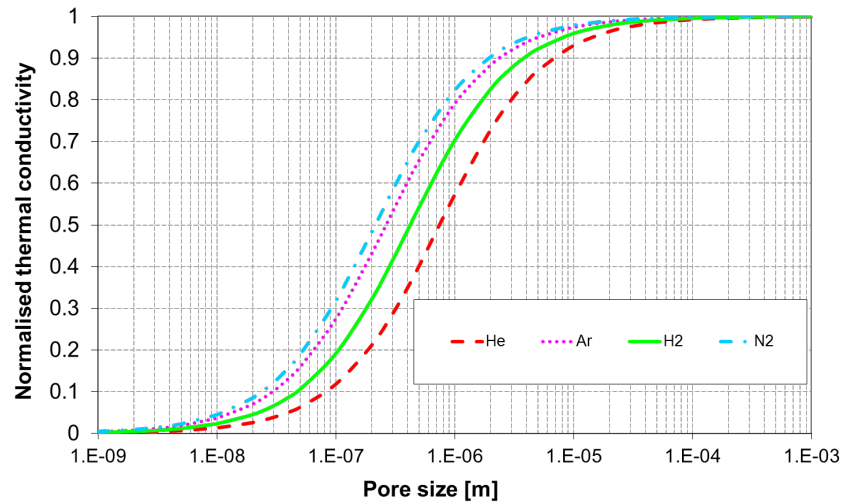
Figure 4. The normalised thermal conductivity of four different gases when inside a pores of different size.

High values (0.75 − 1) of η could means that there are several closed pores and/or several lamellar pores parallel to the surface thinner than 0.1 μm and/or spherical and/or cylindrical pores. To select among the different possibilities also the absolute value of the thermal diffusivity should be considered.

If η is measured both before and after any heat treatment, it can provide indication of the sintering phenomena occurring in the TBC. In particular, an increase of η could be ascribed by:

- an increase of closed pores;
- an increase of very thin pores;
- a reduction of horizontal inter-lamellar pores.
- a spheroidization of pores.

High temperature exposure usually promotes the spheroidization of pores and the partial or complete sintering of the finest fraction of inter- and intra- lamellar pores. On the contrary, it is unusual to observe an increase of very fine pores and cracks especially for free standing coatings. Obviously, partial sintering could also close some path towards pores increasing the volumetric fraction of closed pores.

Thus an increase of η can be mainly ascribed to reduction/spheroidization of inter-lamellar pores and perhaps an increase of the close pore fraction.

According to this foreword, it is worth noting the monotonic increase of η vs. the heat treatment temperature for very porous YPSZ TBC samples, as shown in Figure 5. This occurrence confirms the progressive sintering taking place when the heat treatment temperature is increased. No significant differences can be observed between the trend of η vs. T for the two sets of samples. This seems to provide indications supporting the hypothesis that the presence of steam does not alter the sintering

kinetics. The values of η for dense highly cracked samples (R267) result always higher than the corresponding one for highly porous (R286, R287 and R320), because of the lower inter-lamellar porosity content.

Another parameter that provides indications on the magnitude of the sintering phenomena taking place in the TBC is the ratio $\vartheta = \alpha/\alpha_0$ of the thermal diffusivity α measured after the high temperature exposure and that α_0 measured in the as sprayed condition. Similarly to η, also ϑ is expected to increase monotonically with time and high temperature exposure. This occurrence has been observed also for the samples studied in the frame of this work and it is worth noting in figure 6 that no significant differences can be observed among the trends for samples exposed in H_2O rich atmosphere and those exposed in air. This outcome supports the hypothesis that the increased steam content does not significantly affects the sintering kinetics. Some further information can be obtained when ϑ vs. η is considered. In fact, the increase ϑ of with constant values of η (see for example Figure 7) can be ascribed to the disappearance of very thin inter-lamellar pores very effective in reducing the thermal diffusivity but not affecting η so much, as previously explained.
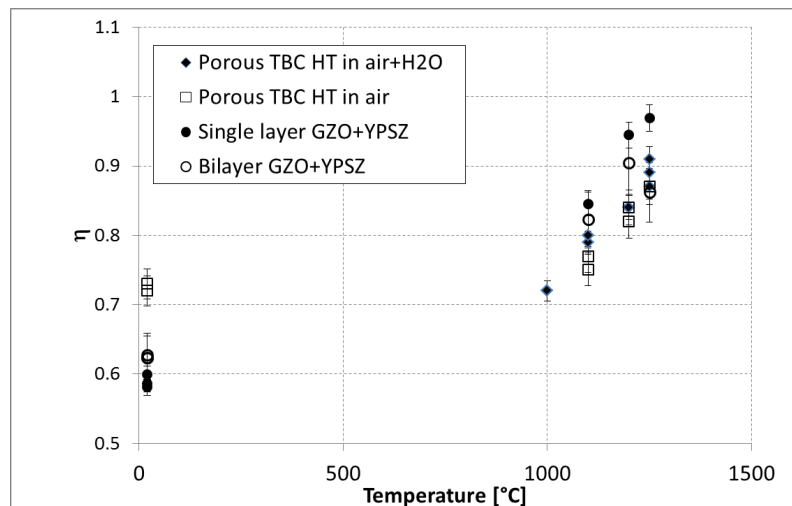

Figure 5. η **vs heat treatment temperature for very porous TBC samples exposed to air+H₂O and air, respectively, and GZO+YPSZ TBCs.**
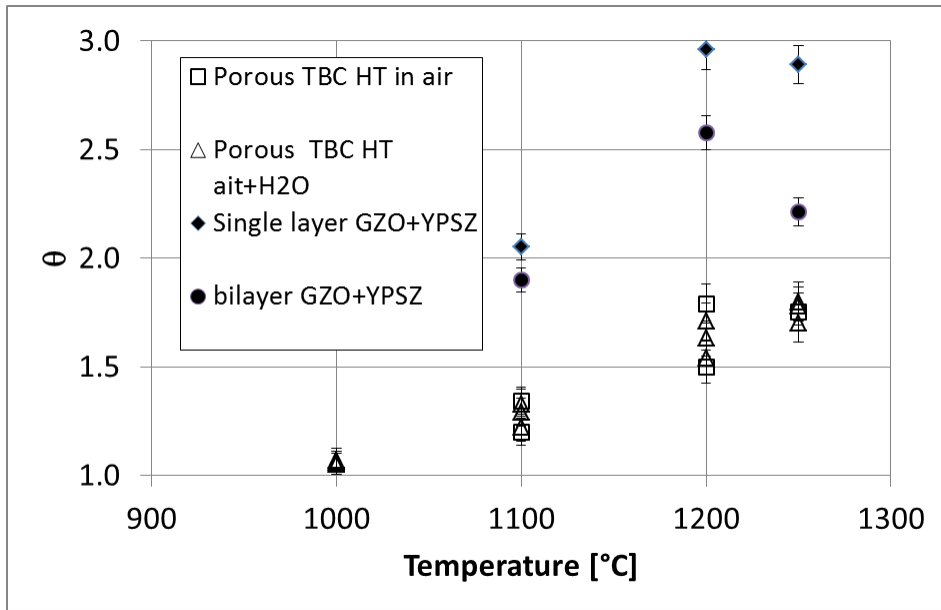
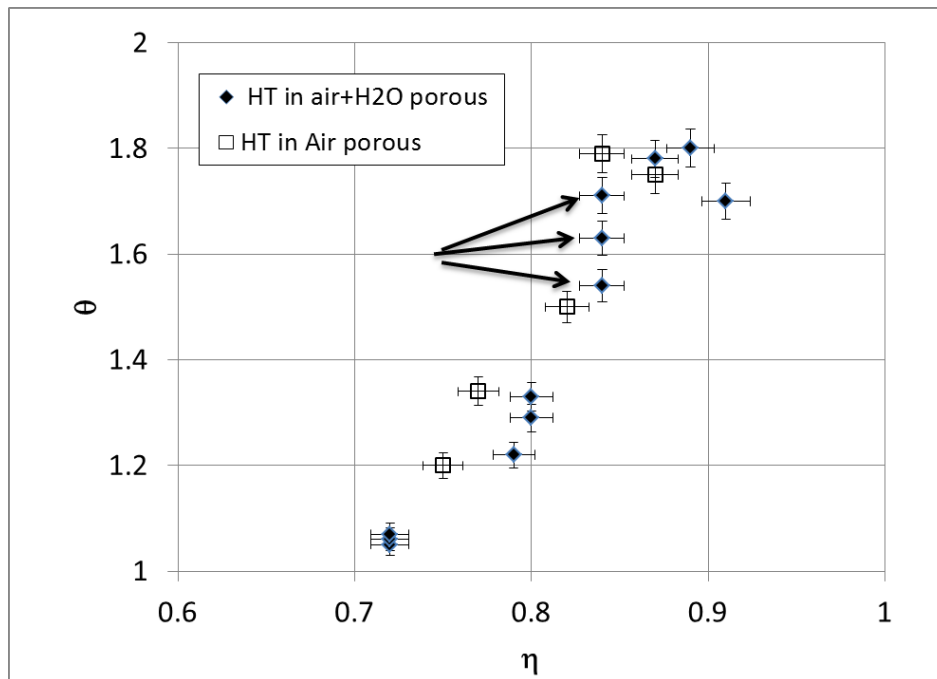**Figure 6.** ϑ vs. heat treatment temperature for very porous TBC samples exposed to air+H₂O and air, respectively.

Figure 7. ratio ϑ of the thermal diffusivity α measured after the high temperature exposure and that α_0 measured in the as sprayed condition vs the ratio η between thermal diffusivity measured in vacuum and in air. Arrows show the different sintering of very fine lamellar pores for three different samples.

Thermal diffusivity as a function of temperature

For each of the two state-of the art TBCs, the thermal diffusivity of has been measured only on one as sprayed sample and one sample exposed to 1250°C for 500 hours in air+20%H_2O atmosphere. Figure 8 summarises the outcomes. As expected, the thermal diffusivity values at high temperatures for aged samples remain higher than those corresponding to samples in as sprayed conditions. It is worth noting that for both highly porous and dense highly cracked samples the thermal diffusivity shows the typical trend as a function of temperature. In particular, for as sprayed samples after an initial decrease vs. temperature typical for materials (such as YPSZ) where phonons are the responsible for the heat transfer, an increase can be observed from about 1000°C, owing to the sintering phenomena starting to take place at high temperature during the measurement.
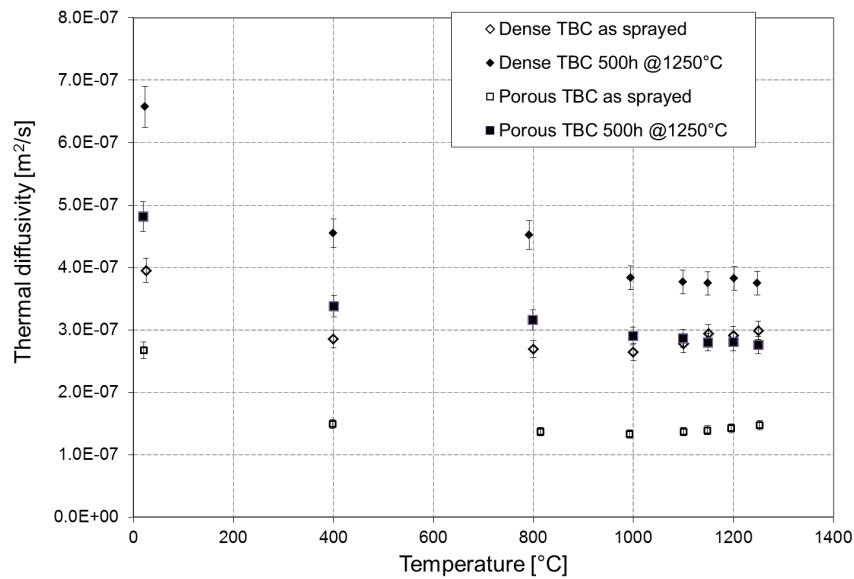

Figure 8. Thermal diffusivity vs. temperature for state-of-the-art YPSZ TBCs both in as sprayed and aged conditions. Measurements have been carried out in vacuum.

Specific heat measurement vs temperature

Specific heat has been measured on an as sprayed TBC (samples R286-1) and on two samples aged in air+20%H_2O atmosphere, as shown in Figure 9.
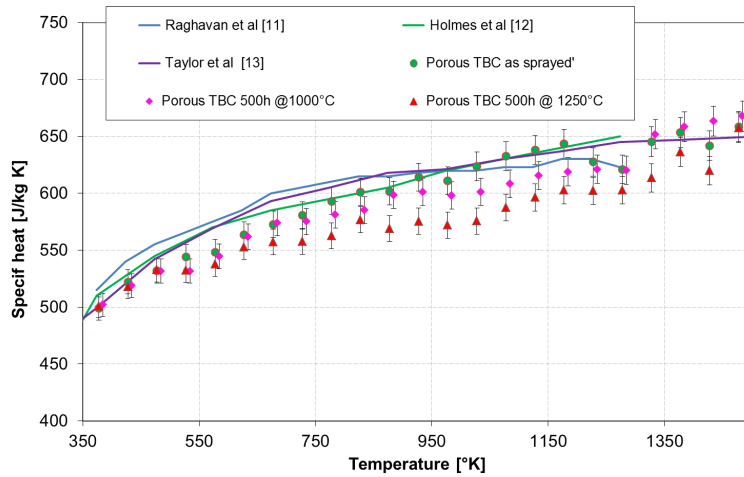
Figure 9. Specific heat vs. temperature for both as sprayed and samples aged at high temperature in air+20% H₂O atmosphere.

The specific heat vs. temperature data reasonably agree with literature, although values for one aged samples resulted slightly below the average [24 - 26]. It is worth noting that according to the literature [27] the specific heat is not expected to change significantly with the stabiliser (Y$_2$O$_3$) content and thus even if phase decomposition occurs during aging, no significant variations of specific heat are expected, as well.

Estimated thermal conductivity vs. temperature

The thermal conductivity k as a function of temperature T has been estimated from thermal diffusivity α, specific heat Cp and porosity f data according to the equation:

$$k(T) = \alpha(T) \bullet C_p(T) \bullet \rho_{th}(T) \bullet (1 - f)$$

for the highly porous and dense highly cracked YPSZ TBCs both in as sprayed and aged conditions, as shown in Figure 10.
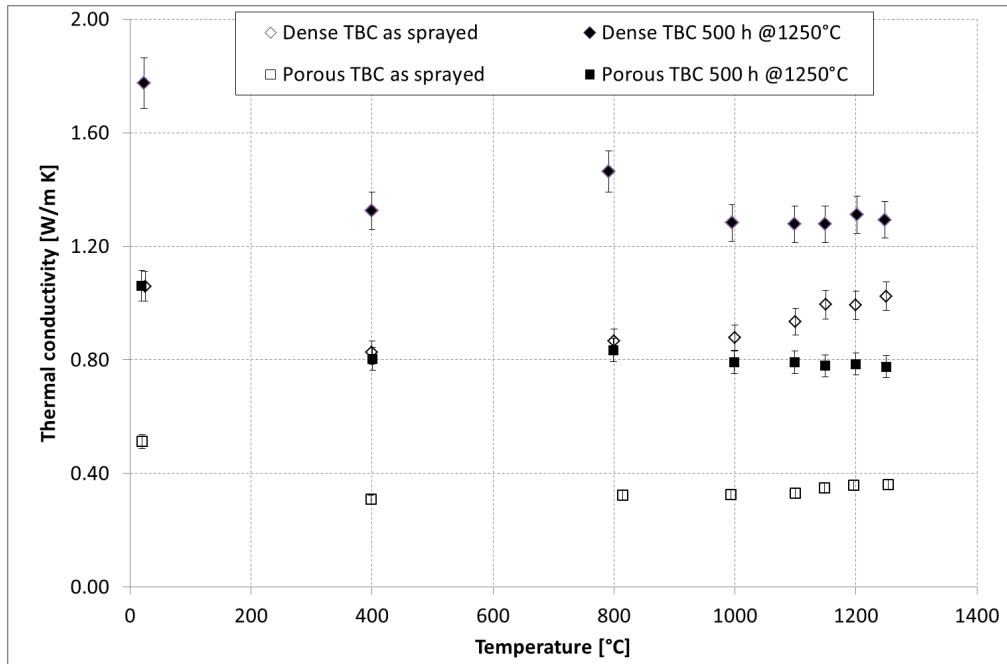
Figure 10. Thermal conductivity vs temperature for state-of-the-art TBC samples.

2.1.3. Advanced TBC

Thermal diffusivity at RT in air and in vacuum

Similarly to the state-of the art TBCs, also for GZO+YPSZ composite samples a characterisation of RT thermal diffusivity has been carried out both before and after high temperature exposure in air.

Table VI and Figures 5-6 summarise the results. It can be observed a monotonous increase of η, the ratio of thermal diffusivity measured in vacuum and in air, as a function of aging temperature for both single and bilayer TBCs. This occurrence seems to indicate that microstructure plays the major role in sintering kinetics, independently from the content of GZO inside the YPSZ TBC.

Furthermore, owing to a high content of lamellar pores parallel to the TBC surface, visible also in Figures 2, for both single and double layer GZO-YPSZ samples, in as sprayed conditions η resulted lower than that of highly porous YPSZ samples, where most of the porosity consists of spherical pores. This interpretation is confirmed also by the slightly lower increase of η with the aging temperature for highly porous samples compared to GZO+YPSZ samples.

Similarly, also ϑ (the ratio of thermal diffusivity after and before the exposure at high temperature) shows a significant increase ranging from 2 to 3 for both single and bilayer GZO+YPSZ samples. As also stated before, this increment greater than that of highly porous the-state-of-the-art TBC can be ascribed to the high lamellar shaped pores content in the advanced GZO+YPSZ samples that is more

prone to sinter (becoming more spherical and sometimes creating healed necks among pore opposite surfaces) compared to spherical pores.

Thermal diffusivity at high temperature

For advanced TBCs thermal diffusivity vs. temperature has been measured only on as sprayed samples both in vacuum and in Ar, as summarised by figure 12.

Since YAG samples have been deposited as amorphous phase, as shown by XRD diffraction patterns of Figure 11, thermal diffusivity has been measured in as sprayed condition and after an heat treatment. In particular, one sample (YAG2) was heat treated 24 hours at 900°C, while the other sample (YAG2bis) was exposed to high temperature just during the thermal diffusivity measurement up to 1100°C.
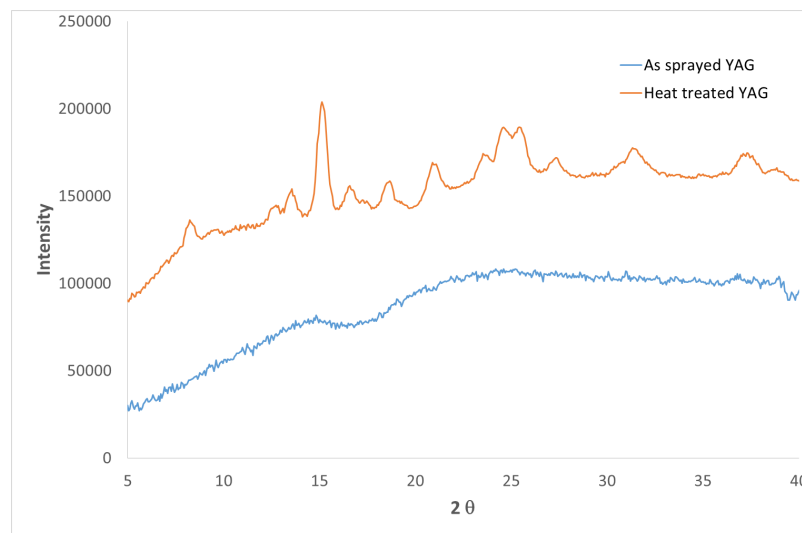

Figure 11. XRD diffraction pattern for as sprayed and heat treated YAG TBC samples.

It is worth noting that single and bilayer GZO+YPSZ TBCs exhibit almost identical thermal diffusivity values and trends vs. temperature, both in vacuum and in air confirming the major role played by the microstructure compared to the different composition. The thermal diffusivity values stay in the lower range for YPSZ samples because of the microstructure and secondarily owing to the presence of GZO that has a lower bulk thermal diffusivity ($6.7 \cdot 10^{-7}$ m^2/s) compared to that YPSZ ($8.8 \cdot 10^{-7}$m^2/s).

According to Figure 12, in the case of YAG, thermal diffusivity in the amorphous phase results one order of magnitude lower than that reported in the literature for bulk single crystal samples ($5 \cdot 10^{-6}$ m^2/s) at RT [28]. After high temperature exposure, thermal diffusivity shows threefold increase for both samples caused by the transition from amorphous to crystalline phase. Thus, the thermal diffusivity of polycrystalline YAG TBCs with a brick-like structure results nearly 3 times smaller than that the single crystal bulk value. It is worth noting that the two heat treatments have been almost equivalently effective in promoting the phase transition. The slight decrease of thermal diffusivity of

the third measurement cycle on sample YAG2bis could be ascribed to some increase of the typical brick-wall like cracking pattern for this TBC occurring during the measurement.
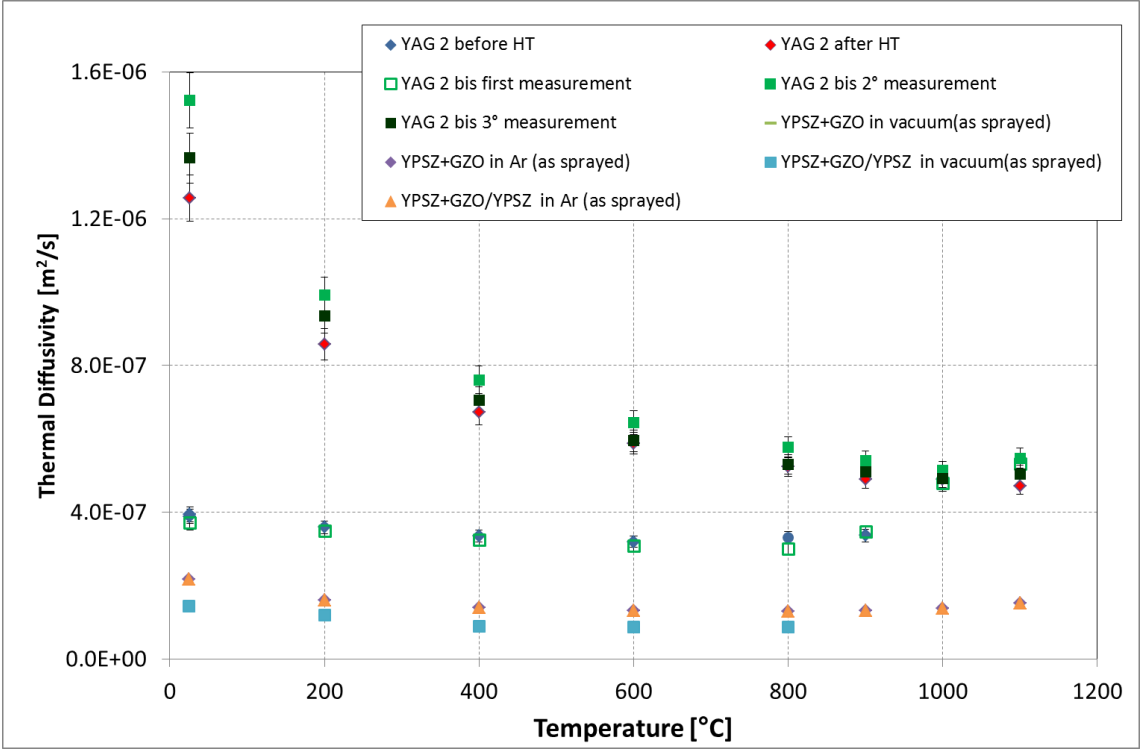

Figure 12. Thermal conductivity vs. temperature for the advanced TBC samples

Specific Heat vs temperature

Specific heat has been measured on one YAG and one GZO sample, respectively, as shown in figure 13.
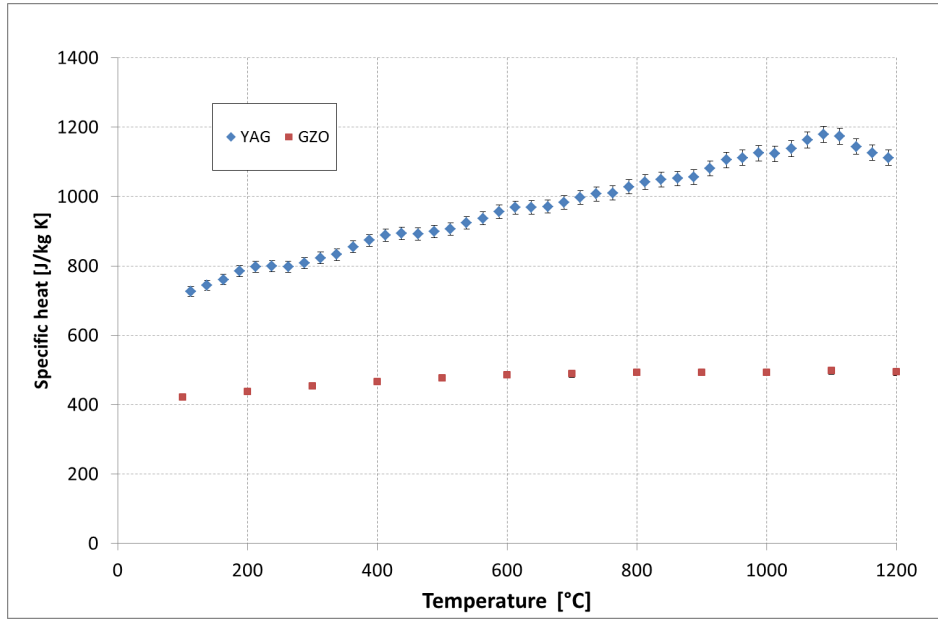
Figure 13. Specific heat vs. temperature for both GZO and YAG samples

Estimated thermal conductivity even vs temperature

Starting from the experimental data, thermal conductivity vs. temperature has been estimated for both GZO and YAG samples, as shown in Figure 14.

Thermal conductivity k has been estimated taking into account that:

$$k = \alpha \bullet \rho \bullet C_p \qquad (1)$$

Density has been estimated from the porosity value f measured by image analysis as:

$$\rho = (f_{YPSZ}\rho_{YPSZbulk} + f_{GdZ}\rho_{GdZbulk})(1 - f) \qquad (2)$$

assuming for YPSZ and $Gd_2Zr_2O_7$ bulk density $\rho_{YPSZbulk}$ and $\rho_{GdZbulk}$ of 6050 and 7000 kg/m³, respectively [29-31]. When density at high temperature has to be considered, according to literature a thermal expansion coefficient equal to $1.1 \bullet 10^{-5}/C^{\circ}$ has been assumed.

For each temperature, a weighted average of the specific heat C_p of both YPSZ and $Gd_2Zr_2O_7$ has been estimated according to image analysis evaluation of the two phases $Gd_2Zr_2O_7$ and YPSZ, after a conversion in weight fractions.

Figure 13 shows the thermal conductivity of both advanced TBCs as a function of the temperature, as measured in Ar and in vacuum. The uncertainty has been obtained by propagating the experimental uncertainty of each parameter in eq.(1) and eq.(2).
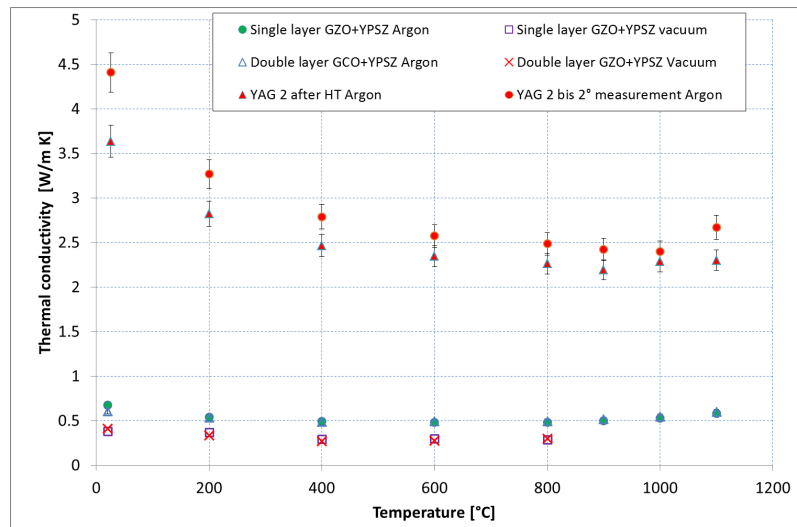

Figure 14. Thermal conductivity vs. temperature for the advanced TBC samples.

It is worth to compare these results with those reported in the literature.

Most of the results reported in the literature refer to dense samples with a very limited amount of closed porosity. Typical values for the thermal conductivity of $Gd_2Zr_2O_7$ resulted about 2/3 of the YPSZ value. In particular at RT $Gd_2Zr_2O_7$ has a thermal conductivity of about 1.6 – 2 W/m K [29, 32, 33] compared to typical values of YPSZ in the range 2.5 – 3 W/m K [27, 29, 34, 35].

The thermal conductivity of the single layer YPSZ-$Gd_2Zr_2O_7$ composite resulted only slightly lower than that of porous state-of-the art TBC studied in the frame of this work (i.e. 0.68 W/mK vs. 0.7 – 0.-8 W/mK). This occurrence could be explained by considering the higher amount of porosity in the state-of-the-art porous YPSZ TBC compared to the YPSZ $Gd_2Zr_2O_7$ composite (30% vs. 15%). Moreover, since the overall content of $Gd_2Zr_2O_7$ does not exceed 65% in volume its contribution to lowering the thermal conductivity is reduced.

YAG thermal conductivity values show a maximum reduction with the temperature by a factor of 0.55. Similarly to thermal diffusivity, both YAG samples exhibit thermal conductivity values roughly one third of the single crystal bulk value reported in the literature [28].

2.4 Synchrotron radiation and standard X-Rays diffraction

The phase evolution of YPSZ APS TBCs samples aged both in air and in air+20%H_2O is summarised in Figure 15 according to the approach proposed by D.Lipkin et al [36] that provided the phase fraction

for the tetragonal *pseudo-t'* phase , Y-rich phases (*t''+c*), Y-lean phase *t* and the monoclinic phase *m*. In particular, to compare phase decomposition data over a wide range of times *t* (in hours) and temperatures *T* (in centigrade degrees) they proposed to use the Hollomon-Jaffe parameter (HJP):

$$HJP = T\big[C + lnt\big]$$

Where C is a constant fixed equal to 27 [36]. The use of this parameter has been adopted in the past either for normalising the extend of thermal diffusivity [37] or the Raman lines [38] owing to sintering phenomena [39] taking place during high temperature exposure.

It is worth remembering that the main outcomes provided by the very detailed and informative studies performed by Lipkin et al [36] and Kronstad et al [14, 39] by coupling Synchrotron radiation diffraction studies with microstructure evolution by TEM analysis can be summarised as follows:

i)   Two competing mechanisms for phase decomposition have been identified in APS TBC: in coarse grains, YPSZ rapidly decomposes into a modulated microstructure of Y-rich and Y-lean domains. On the other hand, in fine grains a grain-boundary precipitation of a Y-rich cubic phase takes place followed by overall coarsening until the tetragonal phase reaches a critical size where it becomes transformable to monoclinic.

ii)   TEM does not confirm the presence of a separate *t'* phase as detected by XRD. This evidence has been explained as an artefact of the coherency strain which gives rise to an average lattice parameter close to that of the original *t'* phase (this is the reason why the XRD-detected phase has been named *pseudo-t'*). When the coherency between Y-rich and Y-lean phases becomes negligible (this occurrence takes place when the Y-lean *t* phase transforms into monoclinic phase) the *pseudo-t'* diffraction peak disappear.

iii)   In consideration to the previous outcomes, it appears clear that depending on the specific microstructure of each single APS TBC one of the two competing phase decomposition mechanisms can prevail over the other hence affecting the phase decomposition kinetics, as shown also in Kronstad et al.[40].

As expected the XRD results on samples analysed in this work show that, the *pseudo-t'* phase and Y-rich, Y-lean and *m* phases decrease and increase monotonically over the HJP range 8000 -51000, respectively. As a matter of fact, in the literature the decrease of the *t-phase* content related to the *t* to *m* transformation is reported to occur at HJP values greater than 51000. The monoclinic phase content in the HJP range analysed in the frame of this work resulted almost negligible for almost the samples apart one.

Furthermore, comparing the phase decomposition evolution for both samples aged in air and in air+20%H_2O, owing to the limited number of samples and the scatter of data, no statistically significant differences can be observed.

It is worth noting that the quantitative phase fraction evolution, as estimated in the frame of this work, is in very good agreement with the literature data obtained for APS TBC samples by Lipkin et al [36], G. Witz et al [41], while it differs a little bit from data provided by Di Girolamo et al [42].
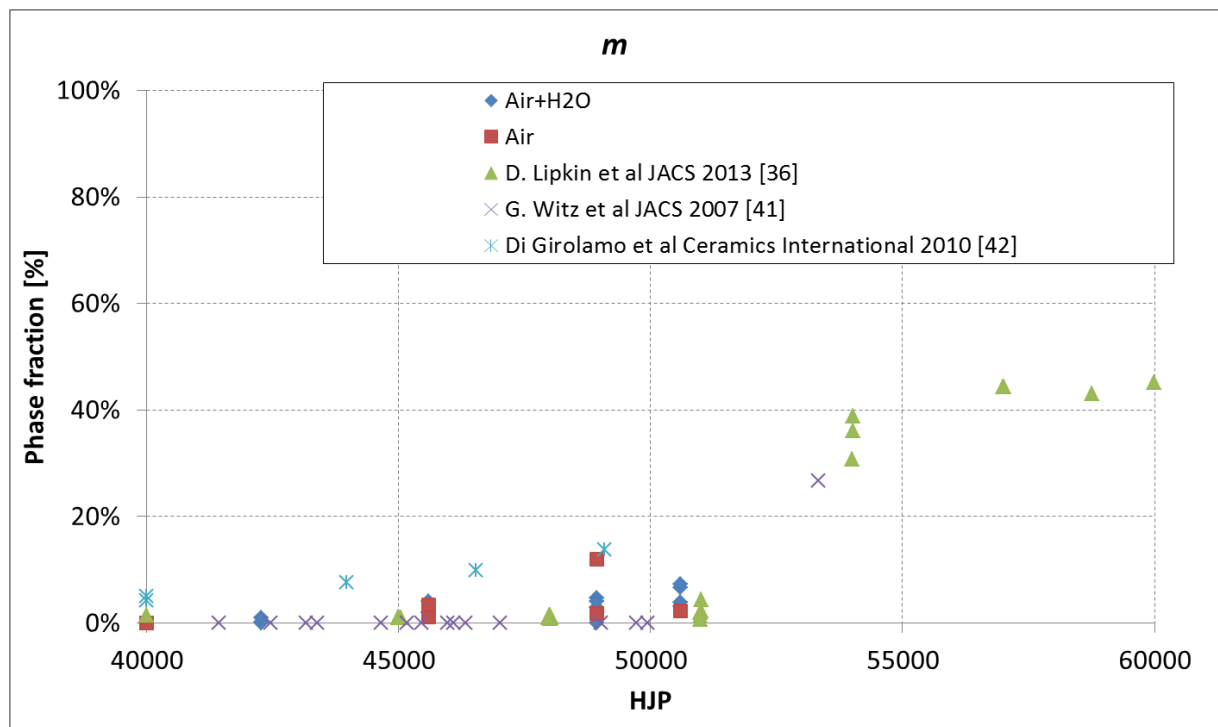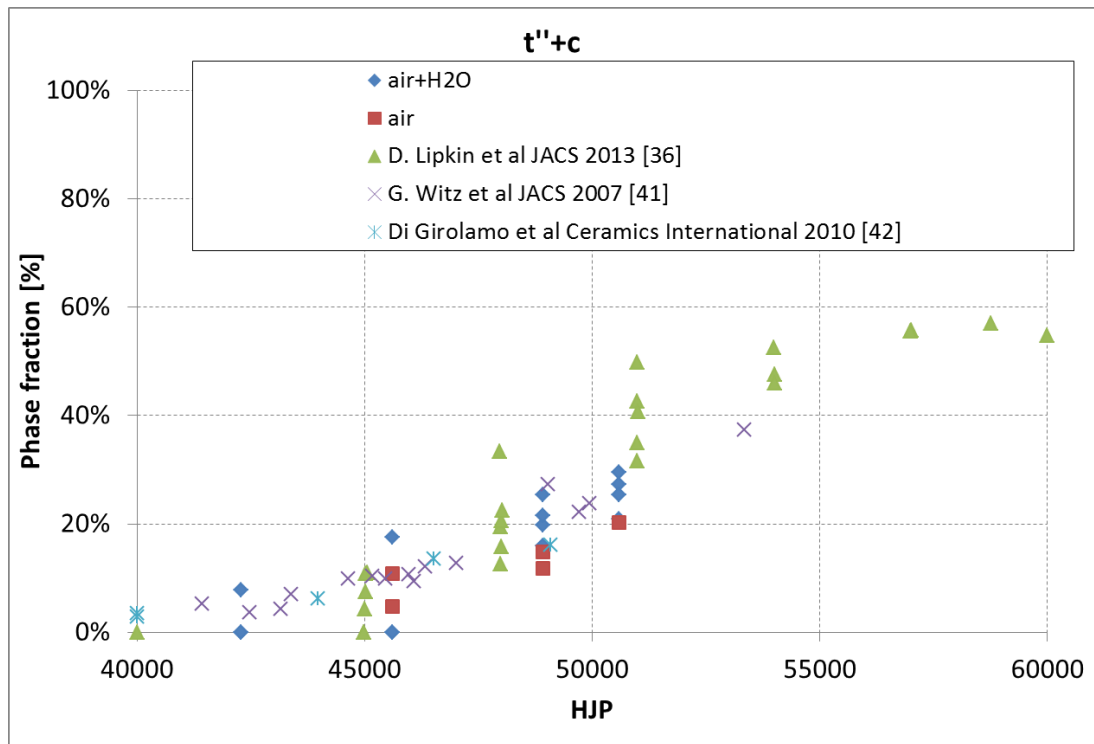
t' phase

t
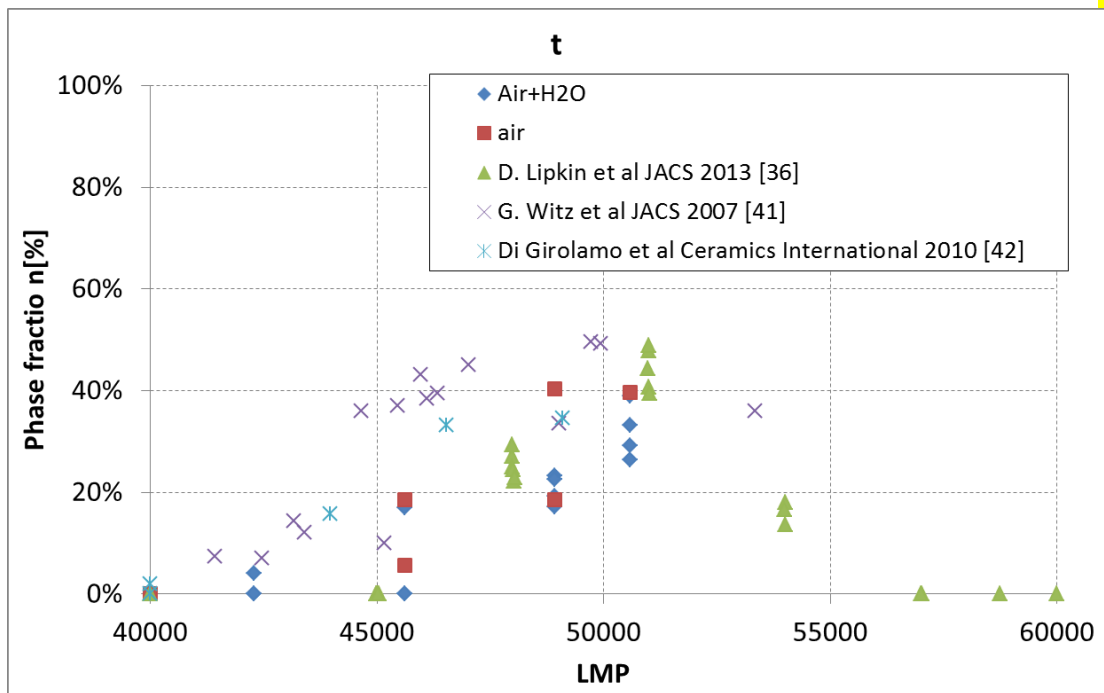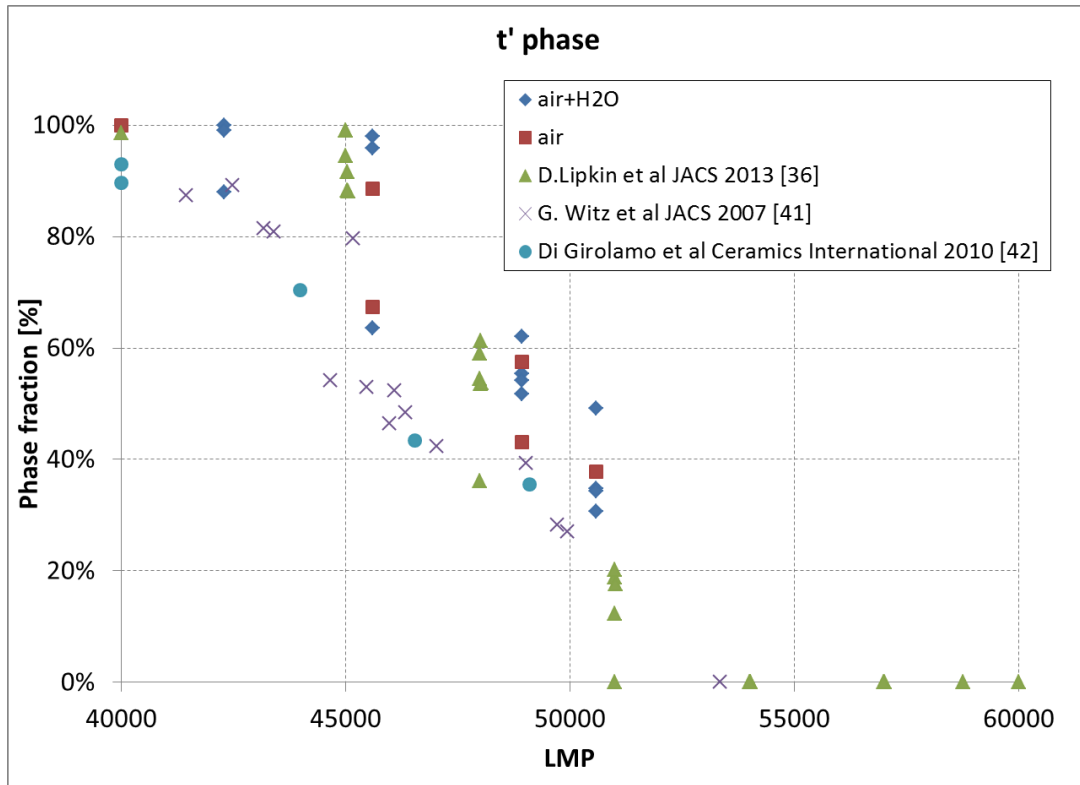
Figure 15 YPSZ samples. Phase fraction evolution vs. HJP. Literature data are also included for comparison.

3. DISCUSSION OF RESULTS

Aging atmosphere seems either not to affect sintering rate of YPSZ TBCs as evaluated by thermal diffusivity data and the related parameters such as η and ϑ or the phase decomposition as evaluated by XRD, at least in the HJP range considered in the frame of this activity. Sintering rate varies

depending on the TBC microstructure. In particular, highly porous TBC with mostly spherical porosity sinter less than TBC with a higher lamellar shape inter-splat pores, such as advanced single and bilayer GZO+YPSZ TBC samples. Furthermore, no significant differences between single and bilayer GZO+YPSZ samples can be highlighted , probably because the microstructure of porous TBCs provides the major contribution to thermal diffusivity, compared to the difference in composition.

As concerns GZO+YPSZ samples, by comparing these results with those reported in the literature for pure $Gd_2Zr_2O_7$ deposited by APS (an overall porosity of only 4.69% is reported) [1] the following comments can be done:

- The thermal diffusivity of both YPSZ and $Gd_2Zr_2O_7$ APS coatings reported in the literature [43] (see Figure 16) are significantly higher than values obtained in the frame of this work, probably because the samples tested in this project have a significantly higher porosity content, especially as concerns inter-lamellar pores.

- Furthermore Moskal et al [43] report an increase of $Gd_2Zr_2O_7$ thermal diffusivity from 800°C up to 1100°C of about 63% which has not been observed neither in the present activity (the increase is limited to 18%) nor in other works in the literature (see figure 16) [32,33]. Moskal et al report an even more significant thermal diffusivity increase for YPSZ that is never been reported in the literature before (see for example [44]). A possible explanation for this unexpected increase could be related to a long permanence time at high temperature during the measurement. In fact just few hours at temperatures higher than 900°C are sufficient to promote the sintering of lamellar porosity (see for example [10, 32]) in YPSZ. As reported in the literature, pyrochloric materials such as $Gd_2Zr_2O_7$ exhibit a less pronounced sintering activity, compared to YPSZ and this can explain the different magnitude of the thermal diffusivity increase observed at temperatures higher than 800°C.

- As concerns the thermal diffusivity decrease from RT up to high temperature, in this work the maximum decrease occurs in the range 800°C – 1000°C and its magnitude ranges from 0.57 to 0.6, as also reported by Liu et al [32, 33]. On the other hand Moskal et al report a reduction up to 0.4 of the RT initial value [43].

The threefold - fourfold thermal diffusivity increase observed for the two YAG samples was caused by the crystallisation from glassy amorphous phase, as pointed out by XRD data. After the first heat

treatment, owing to the dense brick-like structure, only a very small thermal diffusivity increase has been observed.

From the extensive microstructural characterisation of TBC in terms of shape, orientation and content of porosity as well as of composition (by XRD and IA for GZO) the modelling of thermal diffusivity of YPSZ and GZO+YPSZ and YAG can be performed by using the Bruggeman model previously successfully applied for such purpose [45] .
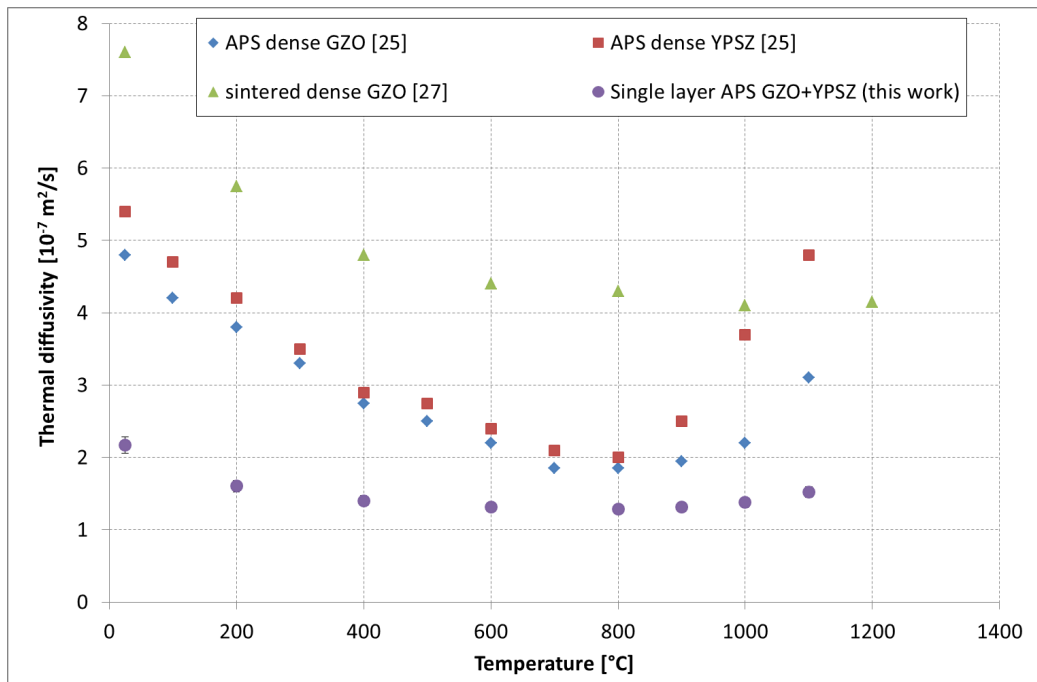

Figure 16. Thermal diffusivity vs. temperature of YPSZ and pure Gd$_2$Zr$_2$O$_7$ deposited by APS [25] or bulk sintered [27]. The single layer of GZO+YPSZ APS as sprayed sample considered in the frame of this work is also included. All measurements have been carried out in Argon atmosphere.

A simulation of the thermal diffusivity at RT have been carried out by modelling: *i*) YPSZ samples considering both porosity features of Table III, the phase composition provided by XRD and the appropriate bulk thermal conductivity values for Y-lean and Y-rich and monoclinic phases according to the literature summarised in Table VII, ii) the single layer two phase porous YPSZ+Gd$_2$Zr$_2$O$_7$ composite TBC. A detailed description of the specific use of the Bruggemann model for this purpose can be found elsewhere [45, 46].

More in details, the two phase material has been considered made of a continuous matrix of Gd$_2$Zr$_2$O$_7$ with a dispersion of YPSZ. The YPSZ dispersion has been considered with an average aspect ratio *a/c*=3 and an orientation of the symmetry axis perpendicular to the sample surface. To simulate the porosity, the data obtained by image analysis and summarized in Tables III and Table IV have been used.

A satisfactory agreement between modelling and experimental results has been obtained, as shown in Figure 17.

A more detailed study should also involve the assessment of the crystallographic phase for $Gd_2Zr_2O_7$ that can be either fluorite-like or pyrochlore-like for the samples under study to better chose the bulk thermal conductivity for the modeling purposes.
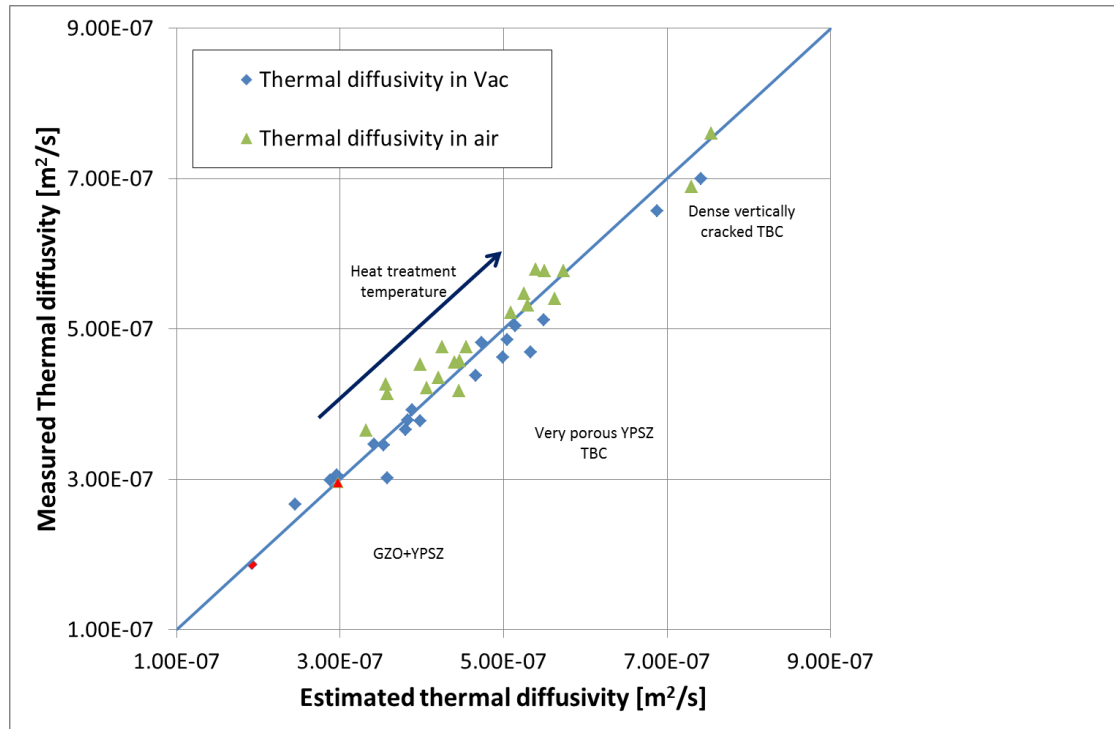

Figure 17. Comparison among experimental RT thermal diffusivity data and the outcomes of the modelling for YPSZ TBC. Red diamond and triangle refer to GZO+YPSZ single layer as sprayed samples.

4. CONCLUSIONS

This experimental activities carried out to investigate the effect of an increased steam content in the aging atmosphere on the state-of-the art YPSZ APS TBC in terms of sintering kinetics and/or phase stability by using thermo-physical and synchrotron radiation diffraction, respectively, did not provide any clear evidence of a different behaviour of TBC, at least in the aging time (500h) and temperature (1000°C-1250°C) range considered in the frame of this work.

As concerns advanced TBCs, thermal conductivity of YSZ-GZO samples are affected mainly by the microstructure and only to a lesser extent by the chemical composition. YAG TBC with the peculiar brick-like microstructure exhibits a high thermal conductivity, compared to YSZ TBC.

5. ACKNOWLEDGEMENTS

To include people from FZJ that measured the Cp of GZO samples

6. REFERENCES

1. Onal, K., Maris-Sida, M.C., Meier, G.H. and Pettit, F.S., "The Effects of Water Vapor on the Oxidation of Nickel-Base Superalloys and Coatings at Temperatures from 700°C to 1100°C", pp. 607-616 in Superalloys 2004, K.A.Green, H. Harada, T.W. Howson, T.M. Pollock, R.C. Reed, J.J. Scherra and S. Walston, editors, TMS, September 19, 2004.

2. J.A. Haynes, K.A. Unocic, B.A. Pint, Effect of water vapor on the 1100°C oxidation behavior of plasma-sprayed TBCs with HVOF NiCoCrAlX bond coatings, Surf. Coat Technol. 215 (2013), 39 – 45.

3. J.A. Haynes, K.A. Unocic, M.J. Lance, B.A. Pint, Impact of superalloy composition, bond coat roughness and water vapour on TBC lifetime with HVOF NiCoCrAlYHfSi bond coatings, Surf. Coat Technol. 215 (2013), 39 – 45.

4. K.A. Unocic, B.A. Pint, Effect of water vapour on thermally grown alumina scales on bond coatings, Surf. Coat Technol. 215 (2013), 30 – 38.

5. M.J. Lance, K.A. Unocic, J.A. Haynes, B.A. Pint, Effect of water vapour on thermally-grown alumina scales on Pt-modified and simple aluminide bond coatings, Surf. Coat Technol. 237 (2013), 2 – 7.

6. M.H. Sullivan, D. R. Mumm, Transient stage oxidation of MCrAlY bond coat alloys in high temperature, high water vapor content environments, Surf. Coat Technol. 258 (2014), 963 – 972.

7. W. Nowak, PhD Thesis at RWTH Aachen 2014.

8. T. Steinke, D. Sebold, D. E. Mack, R. Vaßen, D. Stöver, A novel test approach for plasma-sprayed coating tested simultaneously under CMAS and thermal gradient cycling conditions, Surf. Coat. Technol. 205 (2010) 2287–2295

9. F. Cernuschi, S. Capelli, C. Guardamagna, L. Lorenzoni, D.E. Mack, A. Moscatelli, Solid particle erosion of standard and advanced thermal barrier coatings, *Wear* 348-349(2016) 43–51.

10. Cernuschi F., Bison P.G., Martinetti S., Scardi P., Acta Mater 2008; 56: 4477 –88.

11. Rebuffi L, Plaisier JR, Abdellatief M, Lausi A, and Scardi P (2014) MCX: A synchrotron radiation beamline for X-ray diffraction line profile analysis. *Zeitschrift fur Anorganische und Allgemeine Chemie* 640, 3100-3106.

12. Larson A.C. , Von Dreele R.B. (1994). General Structure Analysis System (GSAS), Los Alamos National Laboratory Report LAUR 86-748.

13. Toby B. H. (2001). EXPGUI, a graphical user interface for GSAS, J. Appl. Cryst. 34, 210-213.

14. J.A. Krogstad, S. Kraemer, , D.M. Lipkin C.A. Johnson, D.R.G. Mitchell, J. M. Cairney, C.G. Levi, Phase stability of t'-Zirconia-based thermal barrier coatings: Mechanistic Insights, J. Am. Ceram. Soc. 94 [S1] S168-S177 (2011).

15. W.P. Parker, R.J. Jenkins, C. P. Butter G. L. Gutter and G.L. Abbott, *J. Appl. Phys.*, 32, pp.1679, (1961).

16. ASTM Standard E1461.

17. R.E. Taylor, K.D. Maglic, *Compendium of Thermophysical Property Measurement Methods* Vol: 1: Survey of Measurement Techniques, Eds. K.D. Maglic et Al. Plenum Press New York 1984.

18. R.E. Taylor, K.D. Maglic, *Compendium of Thermophysical Property Measurement Methods* Vol: 2: recommended Measurement Techniques and Practices, Eds. K.D. Maglic et Al. Plenum Press New York 1992.

19. D. Schwingel, R. Taylor, T. Haubold, J. Wigren, C. Gualco, Surf. Coat. Technol. 108 – 109 (1998), 99 – 106.

20. P. Bison, F. Cernuschi, S. Capelli, Surf. Coat. Technol. 205, 2011, 3128-3133.

21. Cernuschi F., Bison P., Moscatelli A., Acta Mater 2009;57: 3460–71

22. D. A. G.Bruggeman, Ann. Physik, 1935;24: 636-64.

23. M. Knudsen, The kinetic theory of gases, 3rd ed., Wiley, New York, 1950.

24. S. Raghavan, H. Wang, W.D. Porter, R.B. Dinwiddie, and M.J. Mayo, Acta Mater. 49 (2001) 169179

25. Holmes, R. R. and McKechnie, T. N. In NASA Marshall Space Flight Center Advanced Earth-To-Orbit Propulsion Technology vol 1, eds. Richmond, R.J., Wu, S.T., 1988, pp. 692–702.

26. Taylor, R. E., Wang, X. and Xu, X., Surf. Coat. Technol., 120- 121, 1999, 89–95.

27. Azzopardi A., Mevrel R., Saint-Ramond B., Olson E., Stiller K., Surf. Coat Technol. 2004; 177 – 178; 131-9.

28. http://www.crystran.co.uk/optical-materials/yttrium-aluminium-garnet-yag.

29. J. Wu, X. Wei, N. Padture, P.G. Klemens, M. Gell, E. Garcia, P. Miranzo, M.I. Osendi, J. Am. Ceram. 85 [12] 3031-35 (2002)

30. G. Suresh G. Seenivasan, M.V. Krishnaiah, P.S. Murti, J. Nucl. Mater. 249, 259-61 (1997).

31. J. Feng, B. Xiao, C.L. Wan, Z.X. Qu, Z.C. Huang, J.C. Chen, R. Zhuo, W. Pan, Acta Mater, 59 (2011) 1742 – 1760.

32. Zhan-Guo Liu, Jia-Hu Ouyang Yu Zhou, J. Mater Sci 43, 3596 – 3603, (2008).

33. Zhan-Guo Liu, Jia-Hu Ouyang Yu Zhou, Int. J. Appl. Ceram. Technol. 6 [4] 485 – 491 (2009).

34. Youngblood G.E., Rice R.W., Ingel R.P., Thermal Diffusivity of Partially and Fully Stabilized (Yttria) Zirconia Single Crystals, J. Am. Ceram. Soc. 1988; 71(4): 255- 60

35. J-F Bisson, D. Fournier, M. Poulain, O. Lavigne, R. Mévrel, J. Am. Ceram. Soc. 83 [8] 1993 – 98 (2000)

36. D.M. Lipkin, J.A. Krogstad, Y. Gao, C.A. Johnson, W.A. Nelson, C.G. Levi, Phase evolution upon Aging of Air-Plasma Sprayed t'-Zirconia Coatings: I-Synchrotron X-ray Diffraction, J. Am. Ceram. Soc. 96 [1] 290-298 (2013).

37. D. Zhu, R.A. Miller, thermal Conductivity and Elastic Modulus Evolution of Thermal Barrier Coatings Under High Heat Flux Conditions, J. Therm Spray Technol 2000, 9(2), 175.

38. A. M. Limarga, J.Iveland, M. Gentleman, D.M. Lipkin, D.R. Clarke, The Use of Larson-Miller parameters to monitor the evolution of Raman lines of tetragonal zirconia with high temperature aging, Acta Mater 59, (2011), 1162-1167.

39. H.E. Eaton and R.C. Novak, Sintering Studies of Plasma-sprayed zirconia, Surf. Coat. Technol. 32, [1-4], 227-36 (1987).

40. J.A. Krogstad, R. M. Leckie, S. Kraemer, J. M. Cairney, D.M. Lipkin C.A. Johnson C.G. Levi, Phase evolution upon Aging of Air-Plasma Sprayed t'-Zirconia Coatings: II-Microstructure Evolution, J. Am. Ceram. Soc. 96 [1] 299-307 (2013).

41. G. Witz, V. Shklover, W. Steurer, S. Bachegowda, Hans-Peter Bossmann, J. Am. Ceram. Soc. 90 (9), 2935 – 2940, (2007).

42. G. Di Girolamo, C. Blasi, L. pagnotta, M. Schioppa, Phase evolution and thermophysical properties of plasma sprayed thick zirconia coatings after annealing, Ceramics International, 36, (2010), 2273-2280.

43. G. Moskal, L. Swadzda, M. Hetmanczyk, B. Witala, B. Mendala, J. Mendala, P. Sosnowy, J. European Ceramic Soc. 32 (2012) 2025 – 2034.

44. F. Cernuschi, L. Lorenzoni, S. Ahmaniemi, P. Vouristo, T. Mäntylä, J. European Ceram. Soc. Vol. 25 . 393 -400, (2005).

45. Cernuschi F., Bison P., Moscatelli A., Acta Mater 2009;57: 3460–71

46. F. Cernuschi, I.G. Golosnoy, P. Bison, A. Moscatelli, R. Vassen, H-P Bossmann and S. Capelli, Acta Materialia 61 (2013) 248 – 262.

47. S. Raghavan, Hsin Wang, R. B. Dinwiddie, W. D. Porter, M. J. Majo, The effect of grain size, porosity and Yttria content on the thermal conductivity of nanocrystalline zirconia, Scripta Materialia vol. 39, 8, 1119-1125, (1998).

48. P. Heydt, C. Luo, D.R. Clarke, Crystallographic texture and thermal conductivity of Zirconia thermal barrier coatings deposited on different substrates, J. Am. Ceram. Soc. 84, [7], 1539-44, (2001).

49. R. Mévrel, J-C Laizet, A. Azzopardi, B. Leclercq, M. Poulain, O. Lavigne, D. Demange, Thermal diffusivity and conductivity of $Zr_{1-x}Y_xO_{2-x/2}$ (x=0.084 and 0.179), J. Eur. Ceram. Soc. 24, (2004), 3081 – 3089.